ELSEVIER

Ultra-lightweight silicon nitride truss-based structures fabricated via UV-assisted robot direct ink writing

Anna De Marzi [a,*], Sarah Diener [b], Alberto Campagnolo [a], Giovanni Meneghetti [a], Nikolaos Katsikis [b], Paolo Colombo [a,c], Giorgia Franchin [a]

[a] Department of Industrial Engineering, University of Padova, Padova 35131, Italy
[b] Kyocera Fineceramics Europe GmbH, Lorenz-Hutschenreuther Str. 81, 95100 Selb, Germany
[c] Department of Materials Science and Engineering, The Pennsylvania State University, State College, PA 16801, USA

ARTICLE INFO

ABSTRACT

Additive manufacturing techniques have gone beyond their reputation for rapid prototype production and are increasingly adopted for the manufacture of functional components comprising high-end materials and intricate lattice structures. Silicon nitride, renowned for its exceptional mechanical properties and thermal stability, has emerged as a promising candidate for lightweight structural applications. Nonetheless, its high refractive index and density have limited the fabrication of highly complex structures using extrusion and photopolymerization based techniques. In this work, a highly reactive silicon nitride-based ink with high solid loading is developed for the fabrication of ultra-lightweight, truss-based structures. By employing a robot UV-assisted direct ink writing process, it is possible to control the printing head orientation, thus overcoming the limited curing depth of silicon nitride-based inks. The failure behavior of the sintered lattice beam structures under 4-point bending loading has been modeled by applying a linear elastic fracture mechanics (LEFM) based approach to the results of finite element (FE) simulations.

1. Introduction

Truss-based structures are known for their excellent strength-weight ratio and are an integral part of various engineering applications; in fact, their lattice-like framework offers exceptional specific mechanical performance while minimizing material usage, making them ideal for lightweight design solutions in aerospace, automotive and structural engineering [1–3].

Traditionally, the fabrication of truss-based structures has posed significant challenges, particularly when employing conventional manufacturing methods such as subtractive or formative manufacturing methodologies. Specifically, subtractive methods comprehend all controlled machining processes that are able to shape a solid block of material by removing parts of it through grinding, cutting or drilling [4]. On the other hand, formative techniques include all those processes which are based on the application of a mechanical stress (i.e., compression, tension or shear) able to cause the deformation of the material into the desired shape (i.e., casting, molding) [4]. Thanks to their well-established procedures, subtractive and formative techniques

have been widely employed for the shaping of different materials (i.e., polymers, ceramics, metals) with relative low costs and large production volumes [5]. Yet, the fabrication of complex shapes, fine features and/or intricate geometries is restricted by the technologies themselves: tools employed by the subtractive techniques are limited in the allowed movements and tool wear, while a significant amount of material is being wasted in the process; formative ones requires for the precise optimization of the molds design and their filling [5,6]. Another potential approach to fabricate truss-based structures which overcome such limitations is represented by the assembling of individual truss elements to construct the desired structure [7]. While this approach offers advantages in terms of design flexibility, low cost and rapid throughput scalable production, it also presents challenges. The fabrication process can be time-consuming, particularly for intricate designs, and may require the development of automated processes through robotic arms to expedite production for the trusses disposition. Additionally, optimizing the connection joints between truss elements is essential to ensure structural integrity and mechanical performance [8].

The rapid development of additive manufacturing (AM) technologies

---

* Corresponding author.
E-mail addresses: anna.demarzi@unipd.it (A. De Marzi), giorgia.franchin@unipd.it (G. Franchin).

has revolutionized the production of complex geometries, offering unparalleled design freedom and efficiency [9]. Indeed, contrary to subtractive and formative methods, AM technologies are based on the fabrication of the desired object by the layer-wise addition of the selected material without need of molds or tools. Nonetheless, the specific printing process requirements and the layer-by-layer approach of traditional AM techniques have been limiting their unique advantages in terms of design freedom and especially of the achievable surface quality: due to the introduction of interfaces between successive layers, the structural integrity and mechanical performance can be compromised, especially under load-bearing conditions.

With these premises, AM technologies able to overcome the layer-by-layer method would represent the best solution in order to control the orientation of the trusses and promote a better load performance of the lattices [10]. A promising approach resides in the combination of two or more AM technologies in a single hybrid manufacturing technique: by exploiting the so called "1 + 1 = 3" effect, the advantages associated to each of the coupled methodologies are exploited, their related drawbacks overcome, and novel capabilities can be unlocked [11]. An example is the UV-assisted Direct Ink Writing (UV-DIW) process, which is a concurrent, assisted hybrid process where a photocurable suspension is extruded through a nozzle and consequently cured by an external UV source. Our previous works [10,12] demonstrated that proper optimization of the ink reactivity and the use of a 6-axis robot arm allow to deposit the material along the direction of the trusses, hence fabricating freeform stretch-dominated structures with enhanced mechanical properties.

In this context, the use of technical ceramics holds a significant promise for the fabrication of high-performance truss-based structures. Silicon nitride, for example, is a non-oxide ceramic material of particular interest for structural applications. It has excellent hardness, strength, and thermomechanical properties, as well as chemical inertness, wear resistance, and both thermal and electrical insulation properties [13,14]. Moreover, compared to other advanced ceramics such as alumina and zirconia, it possesses a lower density and a lower thermal expansion coefficient. Therefore, it is particularly used in machining and bearing applications, automotive engines parts, aerospace components and medical devices [15–17]. Several AM techniques have been proposed for the fabrication of silicon nitride components [18], including Selective Laser Sintering (SLS), Fused Filament Fabrication (FFF), Direct Ink Writing (DIW) and Digital Light Processing (DLP) [19–22]. Nonetheless, the high density and weak Coulomb repulsion forces characterizing the Si_3N_4 powders limit its dispersion both in slurries [23,24] and thermoplastic matrices [25], thus making processes such as DIW, DLP and FFF rather complex. In addition, the strict rheological requirements and the limitations in producing suspended features and/or severe overhangs with DIW and FFF restrict the range of printable shapes to either bulky monoliths or thin-walled structures (i.e., scaffolds, honeycombs) [26,27]. While DLP could represent the best alternative in terms of printing resolution [28], the light-particle interaction plays a major role – due to the high refractive index possessed by Si_3N_4 – as it hinders light penetration and activation of the photocurable moieties, leading to exceedingly long exposure times to guarantee adequate bonding between the cured layers [22,23].

Here we explore the fabrication of ultra-lightweight silicon nitride truss-based structures via robot UV-assisted direct ink writing. Despite its potential, the current state of the art has not fully harnessed the capabilities of the UV-DIW hybrid system, particularly for the fabrication of technical ceramic components. This research seeks to extend the hybrid AM approach to silicon nitride, whose challenging features could offer the opportunity to further validate and optimize the UV-DIW approach. To this aim, a photocurable suspension containing 50 vol% of silicon nitride is obtained by modifying the particles surface and selecting a high-functional acrylate. The freeform ability of the ink is confirmed by analyzing the ink rheology and curing behavior, ultimately confirming that truss-based structures can be fabricated despite

the limited curing depth of Si_3N_4. After having experimentally tested the sintered lattice beam structures under 4-point bending loading, the failure behavior and maximum loads have been estimated by applying a linear elastic fracture mechanics (LEFM) based approach to the results of finite element (FE) simulations. The LEFM approach consists in a combination of the averaged Strain Energy Density (SED) [29], which is particularly suitable when dealing with the static failure of brittle materials, with the Peak Stress Method (PSM) [30,31], which is a rapid, FE based method to estimate the parameters of the local, singular stress fields.

2. Materials and methods

2.1. Particles surface modification

The silicon nitride powder was supplied by Kyocera Fineceramics Precision GmbH (Germany) and consisted of Si_3N_4 particles with Al_2O_3 and Y_2O_3 as sintering aids (Figure SI 1 (a)). The particle surface was modified to decrease the overall viscosity of the ink and increase powder dispersion. Therefore, 6.3 wt% of the powder mixture was firstly dispersed in water with 1 wt% of an amino alcohol-based cationic dispersant (Dolapix A88, Zschimmer & Schwarz, Germany) and 1 wt% of 3-glycidyloxypropyl trimethoxy silane (Dynasylan® GLYMO, Evonik, Germany); weight amounts are calculated with respect to the solid content. To allow for the absorption of the silane agent onto the particle surface, the slurry was mixed by ball milling at 1800 rpm for 15 min and the procedure was repeated for a total of 15 cycles. After drying at 80 °C for 20 h, the powder was manually pestled to break down any agglomerates that might have formed. Finally, the surface-modified silicon nitride powder was sieved (< 90 μm).

2.2. Ink preparation and characterization

The ink results from the addition of the surface modified Si_3N_4 powders to a mixture of trimethylolpropane triacrylate (TMPTA, Sigma Aldrich, Germany), i.e., the photopolymer, and 2-phenoxyethanol (POE, TCI Chemicals, Japan), i.e., the solvent; due to the wavelength of the UV LEDs and to its radicals forming efficiency, bis (2, 4, 6-trimethyl benzoyl)-phenyl phosphine oxide (Omnirad 819, IGM Resins, Netherlands) was selected as the photoinitiator and later added into the mixture. The ink composition is listed in Table 1.

To promote better homogenization and dispersion of the solid particles into the liquid mixture, the required amounts of the two Si_3N_4 powder size ranges distributed following the Bolomey equation (see Supporting data), were added in a stepwise process (36 – 75 μm and 75 – 90 μm, in sequence). Each step was followed by a mixing step of 4 min at 2000 rpm using a centrifugal mixer (DAC 250.4 VAC-P LR, Hauschild SpeedMixer®, Germany), and ABS balls with a diameter of 6 mm were introduced into the container during the mixing step to further facilitate the dispersion of the solid particles and prevent their agglomeration.

The obtained ink was then stored under dark conditions and added to a syringe. Prior to printing, a defoaming step at 2200 rpm for 5 min (ARE-250, THINKY, Japan) was performed to release the air entrapped during the syringe loading procedure, thus preventing discontinuity of ink extrusion during printing.

The rheological behavior of the ink was analyzed using a rotational rheometer (Kinexus Lab+; Netzsch, Germany). The instrument was

Table 1
Silicon-nitride-based ink composition.

Reagent	Relative amount [vol%]
Si_3N_4 functionalized powders	49.6
TMPTA	37.3
POE	12.4
Omnirad 819	0.7

equipped with a 40 mm plate-plate geometry and a gap of 0.7 mm; measurements of shear stress and viscosity were performed over a shear rate range of 0.1 to 150 s^{-1}. For photo-rheological characterization, a UV-plate system accessory (KNX5007, Netzsch, Germany) with a 40 mW cm^{-2} UV lamp was used. The analysis employed an 8 mm parallel plate geometry and a gap of 0.5 mm. A three-interval thixotropy test (3ITT) was conducted to monitor shear viscosity evolution: (i) 0.5 % strain for 30 s at 1 Hz, (ii) 100 s^{-1} shear rate for 30 s, and (iii) 0.5 % strain for 5 min at 1 Hz. During the last step, the UV light was switched on for 1 s at varying light intensities (70 mW cm^{-2}, 150 mW cm^{-2} and 270 mW cm^{-2}).

The UV light intensity was measured using a UV power meter console (PM400, Thorlabs Inc., USA) coupled with a photodiode power sensor (S120VC, Thorlabs Inc., USA).

A micrometer screw gauge was used to determine the curing depth of the suspension and the thickness of the cured section of ink droplets irradiated by the UV-LEDs at varying exposure times (with the light intensity fixed at 70 mW cm^{-2}) or varying light intensities (at 1 s and 5 s). The corresponding energy densities were calculated as the product of light intensity and exposure time.

2.3. UV-DIW setup and printing process

The UV-DIW printing setup consists of a dispensing unit – comprising of an extruder (vipro-HEAD 3, ViscoTec Pumps and Dosing Technology GmbH, Germany) and a UV-blocking nozzle tip (interior Ø 0.84 mm, Vieweg GmbH, Germany) – installed as the end-effector on a 6-axis industrial robot (RV-4FRL-D, Mitsubishi Electric Corporation, Japan), using an aluminum support. A syringe barrel (30 cc, Vieweg GmbH, Germany) containing the material, under a gas pressure of 2 bar, was connected to the dispensing unit and fed into the extruder.

To allow for the rapid curing of the photocurable ink exiting from the nozzle during printing, the dispensing unit was equipped with an array of 15 UV diodes (UV5TZ-400–15, Bivar Inc., USA) attached to a custom printed circuit board (PCB), with an intensity of 70 mW cm^{-2}, measured at a wavelength of 400 nm, at the point of extrusion. Such UV-LED diodes are evenly distributed around the nozzle tip using a custom 3D printed add-on (Figure SI 3).

An extensive description of the system architecture is presented in our previously published work [10] and summarized in the Supporting data (*UV-DIW setup*). Specifically, the fabrication of components through the UV-DIW setup is enabled through the use of a custom graphical user interface (GUI) that allows simultaneous control of the robot movements and switching operations related to the extruder and UV-LEDs using the robot software RT Toolbox 3 (Mitsubishi Electric Corporation, Japan) and a PLC (EK1100, Beckhoff Automation GmbH & Co. KG, Germany) with its modules (for the extruder and UV-LEDs respectively, EL7370 and EL2808, Beckhoff Automation GmbH & Co. KG, Germany).

2.4. Heating treatments

To remove the organic phase and achieve complete densification, all samples were debinded at 560 °C for 1 h in air and then sintered at 1780 °C with a holding time of 2.5 h in a nitrogen atmosphere. For both thermal treatments, custom-made furnaces from FCT Systeme GmbH (Germany) were used.

2.5. Samples characterization

A comparison between the printed samples and the starting CAD model was performed measuring the thickness and inclination of horizontal, vertical and diagonal beams from optical stereomicroscopy images (AxioCam ERc 5 s Microscope Camera, Carl Zeiss Microscopy, Oberkochen, Germany) using a Java-based image processing program (ImageJ, NIH, USA) [32]. The images were collected from 12 different

lattice structures, for a total of 36 beams analyzed. The cross section of the printed filaments was also observed.

Thermogravimetry analysis (TGA/DSC 3 +, Mettler-Toledo S.p.A., Italy) on printed (extruded and cured) filaments was carried out in static atmospheric air from room temperature to 900 °C, with a heating rate of 10 °C min^{-1}.

The bulk and apparent densities of the components were calculated according to the Archimedes principle by using an analytical electronic balance having a resolution of 0.1 mg (Sartorius 1801, Sartorius GmbH Göttingen, Germany). The values were obtained from measuring 23 different sample weights under dry and immersed conditions, using distilled water as liquid medium [33].

The sintered components were observed by scanning electron microscopy (TESCAN SOLARIS, TESCAN, Czech Republic) at 5 keV and magnifications of 15000X and 72500X.

X-ray diffraction analysis (Bruker AXS D8 Advance, Bruker Corp., Italy) was performed on the silicon nitride powder and on the sintered samples. The voltage and current settings of the diffractometer were set to 40 KV and 40 mA, respectively. The scan angle ranged from 10° to 80° with a scan speed of 1 scan s^{-1} and step size of 0.05°.

The mechanical properties of the sintered lattice beam structures were tested in a 4-point bending test using a universal testing machine (Schenck Trebel, Darmstadt, Germany) with a crosshead speed of 0.7 mm/min until the failure of the sample. Load-deformation curves have been obtained considering the relative movement of the loading pins in the vertical direction, starting upon contact between the pins and the specimens, detected at a minimum load of 5 N.

A total of 11 samples were tested; their fracture load was registered and then processed to calculate the flexural strength; the variability of flexural strength was analyzed using the two-parameter Weibull distribution [34].

2.6. Linear elastic fracture mechanics (LEFM) based approach combined with finite element structural simulations to estimate the experimental fracture loads

The fracture load of the sintered lattice beam structures under 4-point bending loading was estimated by applying a linear elastic fracture mechanics (LEFM) based approach and compared with those derived from experimental tests. To this aim, 4-point bending tests of the lattice beam structures were simulated by adopting the Ansys® Mechanical Finite Element (FE) code. An isotropic, linear elastic material behavior, having E = 300000 MPa and ν = 0.3 (i.e., typical for silicon nitride), was given as input to Ansys® FE code.

The ideal CAD geometry of the lattice beam structures, which was updated to account for the final dimensions after sintering, was analyzed; moreover, also the pins of the 4-point bending fixture were included in the FE model to properly simulate the load transfer to the lattice structure. A 3D, tetrahedral, 10-node, SOLID 187 finite element was adopted to discretize the lattice beam structures; while, a 3D, brick, 20-node, SOLID 186 was used for the pins.

Following the LEFM-based approach provided in the Supporting data, the maximum element size which can be adopted to generate the mesh pattern is $d_{max} = a/3 = 0.2$ mm, with a being the beam diameter which equals 0.6 mm. Therefore, for comparison purposes two different element size d were adopted to generate the mesh pattern, i.e., $d = 0.1$ mm and 0.2 mm (shown in Figure SI 5) for which a maximum opening peak stress $\sigma_{peak} = 622$ MPa and 454 MPa, respectively, is expected at failure according to equation (SI 1). Afterwards, the boundary conditions were applied as sketched in Figure SI 6, where:

- the remote displacement U_y was applied to the surface of the upper pins;
- the surfaces of the lower pins were fully constrained, i.e., displacements U_x, U_y and U_z were set to zero;

- frictionless contact surfaces were defined between the upper pins and the neighboring beams as well as the lower pins and the neighboring beams.

Then, the FE model was solved. After the solution, the load applied to the lattice structure was calculated as the reaction force R_y generated at the lower fixed pins. The applied displacement U_y was iteratively modified until the maximum principal stress σ_{peak}, calculated at the critical point of the structure was coincident with that derived from equation (SI 6) for the relevant element size d. The corresponding reaction force R_y was defined as the numerically estimated failure load compared with the experimental ones.

3. Results and discussion

3.1. Ink design, printing and freeform ability

As previously described, the printing process of the UV-DIW technique is based on the extrusion of a photocurable ink. Specifically, for the work presented here, the ideal feedstock is represented by a well-dispersed suspension of silicon nitride particles; it should possess a shear thinning behavior, even at high particle loading, thus ensuring a stable flow through the nozzle at moderate shear rates during printing; at the same time, it should reacts rapidly upon irradiation and retain the extruded shape [35,36].

According to the power law model, the rheological behavior of a non-Newtonian fluid can be described according to:

$$\sigma = K\gamma^n \tag{1}$$

where σ and γ represent the shear stress and shear rate, while K and n are respectively the consistency index and the power law index of the fluid equation [37]. Fig. 1 shows the viscosity and shear stress profile of the silicon nitride-based ink: by interpolation with (1) it is possible to obtain characteristic values of $K = 2.6 \pm 0.3$ Pa s^n and $n = 0.11 \pm 0.01$ ($R^2 = 0.99$), thus indicating an ink possessing a significant shear-thinning behavior (i.e., $n < 1$), well aligned with the process requirements.

The rapid consolidation of the ink, however, depends on the photopolymerization of the polymer network, which usually consists of a mixture of acrylate monomers and/or oligomers with photoinitiators.

The reactivity of the photocurable part is correlated to the critical light energy dose required to start the polymerization reaction, which directly influences the curing depth of the ink. This effect can be described by considering the relationship proposed by Griffith and Halloran based on the Beer-Lambert law [38]:

$$C_d \alpha \frac{d}{\phi} \frac{1}{Q} \ln\left(\frac{E_0}{E_c}\right) \tag{2}$$

where the curing depth (C_d) of a loaded photocurable suspension is proportional to the average particle size (d) and the exposure energy dose (E_0), while it is inversely proportional to the volume fraction of the ceramic particles (ϕ), the critical energy (E_c) and the scattering ability of the suspension (Q). As the acrylate mixture represents the main solvent in which the ceramic particles are suspended, Q represents the refractive index (RI) difference between the ceramic particles and the photocurable phase ($Q \alpha \Delta n^2 = (n_{ceramic} - n_{solution})^2$). From equation (2), since adequate solid loadings are necessary to readily sinter dense ceramics, it follows that high penetration depths can be achieved only by fine matching the RI of the reagents. In addition to that, a limited mismatch of the RI is also associated to a good dispersion of the particles in the solvent phase. In fact, the Van der Walls forces which govern the attraction between two identical particles [39] can be expressed as:

$$F_{VdW} = \frac{-Aa}{6\pi h}, \text{ with } A = f\left(\varepsilon^2, \Delta n^2\right) \text{ and } \varepsilon = f(n) \tag{3}$$

where ε is the dielectric constant and n the refractive index. When particles and medium matches their refractive indexes, both terms of A become negligible, thus minimizing the Van der Walls attraction forces; hence, as a minimum in free energy at the equilibrium thickness is reached, particles agglomeration is avoided and so is a dramatic increase in the ink viscosity [40,41]. However, it should be considered that the tuning of the RI mismatch of silicon nitride-based inks is not trivial: due to the higher RI value possessed by Si_3N_4 with respect to the one of acrylates (i.e., $n_{Si3N4} = 2.03$ and $n_{acrylates} = 1.46$), the curing depth is negatively affected by Q. In addition to that, it should be noted that, due to their grey color, silicon nitride particles have also a large absorbance value, thus negatively affecting the curing behavior [42].

Starting from such considerations, the ink design strategy followed two different routes. On one hand, TMPTA was selected as the photocurable phase: due to its high functionality, its curing mechanism can more easily compete against the absorption of the light by the dark Si_3N_4 particles, thus promoting the creation of a strong polymer network in the ink upon curing [43,44]. On the other hand, a silane coupling agent was introduced in the starting suspension, which is adsorbed on the surface of silicon nitride particles and keeps them separate through steric hindrance. Indeed, Liu et al. [22], demonstrated that Dynasylan® GLYMO decreases the overall viscosity of the Si_3N_4 based ink by increasing the particles dispersion thanks to the chemical adsorption of the silane agent onto the particle surfaces. Covering the surface of Si_3N_4 particles with silanol groups results also in an enhanced curing depth thanks to the tweaking of the refractive index (GLYMO has a RI of 1.43): as reported by Huang et al. [45], a similar effect could be also achieved by oxidation of the silicon nitride powders, thus forming an amorphous SiO_2 layer on the surface. Finally, POE was added to the ink as non-photocurable solvent: thanks to its hydroxyl group, it acts as a solvation agent by interacting with the OH groups covering the surface of the modified Si_3N_4 powders, thus facilitating the dispersion of silicon nitride particles [40]. This strategy allowed to maximize the silicon nitride content in the ink up to 50 vol% (corresponding to 73.9 wt%) while preserving homogeneity and UV reactivity. Such value is significantly higher compared to other previously published works on the vat photopolymerization (i.e., 40 vol% [46]) and UV-DIW (i.e., 50 wt% [47]) of silicon nitride-based components, and is expected to increase the final density of the components after sintering.

Fig. 2 (a) reports the experimental values of curing depth of this ink as function of the exposure time using a light intensity of I = 70 mW cm^{-2}. Most literature on the DLP of Si_3N_4 components reports really poor curing depths caused by the RI mismatch, limiting the printability [23,43,48]; the values measured in our work are about 5–40 % higher
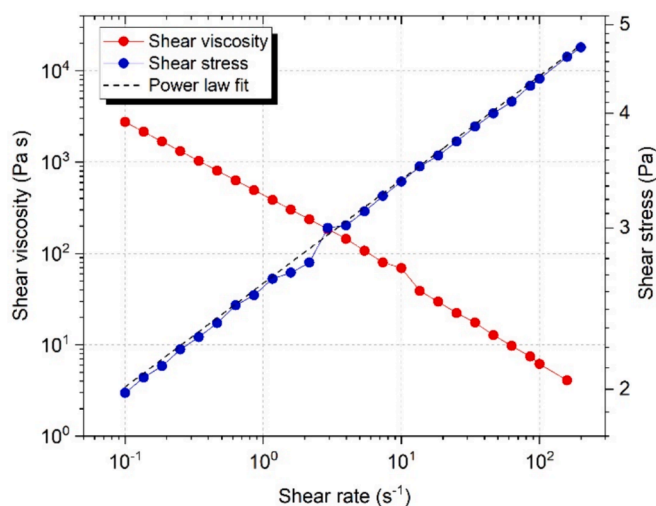

Fig. 1. Viscosity and shear rate profile as a function of shear rate with interpolation by the power law model.
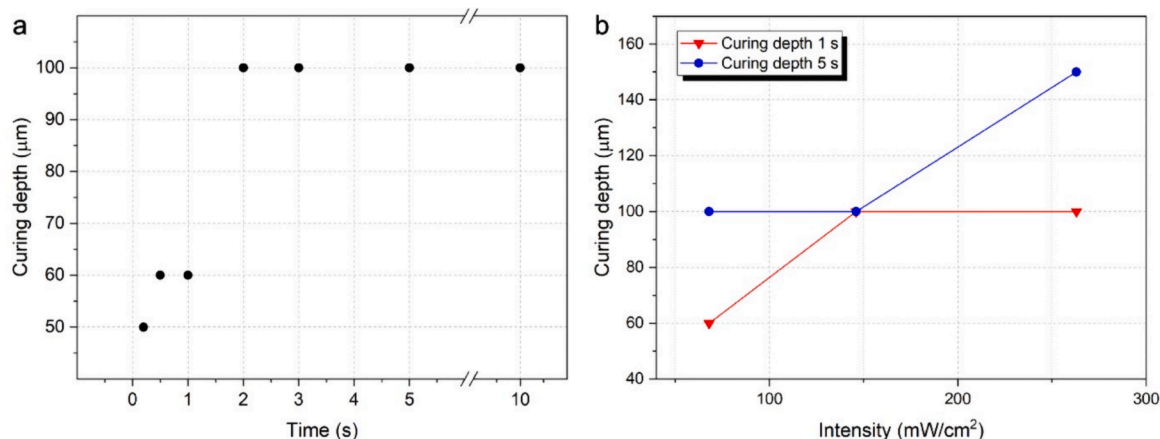
Fig. 2. Curing depth of the silicon nitride ink as a function of (a) exposure energy density (logarithmic scale) and (b) UV light intensity; 1 s (blue line, triangles) and 5 s (red line, circles).

when compared to other inks with similar Si_3N_4 volume concentrations [23,47,49]. Indeed, this can be attributed to the introduction of GLYMO: while on one end the polymer chain is adsorbed on the particle surface, on the other chain end the epoxy group reacts with the acrylate, creating a bridge that lowers the Q parameter in (3), consequently increasing the curing depth [22]. As expected, an increased curing time result in an increased cured thickness; however, two distinct plateaus in the curing depth are detected – 60 μm for t < 1 s and 100 μm for t > 5 s –, suggesting a non-linear correlation and thus limiting the use of the Jacobs equation typically employed for predicting the characteristic curing values for the ink (i.e., critical energy dose and penetration depth) [50]. Similar observations were reported by Shen et al. [51], Li et al. [52] and Chartier et al. [53], which attributed such plateaus to a secondary monomer-to-polymer conversion process promoted by the light scattering. Specifically, they suggest that even if the UV light does not penetrate below a certain depth, further exposure of the cured layer can lead to a decaying of the light which extends the polymerization to the un-cured part of the ink [54]. The phenomenon depends not only on the amount of un-reacted monomers present underneath the polymerized layer, but especially on the energy dose. This was verified by measuring the evolution of the curing depth as a function of the light intensity for two different exposure times. As shown in Fig. 2 (b), a higher curing depth (150 μm) compared to the ones previously reported could be reached only after 5 s of exposure at 270 mW cm^{-2}; such high intensity values can be difficult to replicate during the printing process from the hardware setup point of view.

The viscosity behavior of the Si_3N_4 ink upon curing was assessed using the three intervals thixotropy test (3ITT), which mimics the different phases occurring during the printing process. Specifically, they correspond to (i) the ink being at rest inside the syringe, before extrusion, (ii) the extrusion of the ink through the nozzle tip, and (iii) the ink after extrusion once the applied force is removed. In Fig. 3 the 3ITT test is reported for two different scenarios, being (i) a conventional DIW printing process with no UV light (black dots), and (ii) the hybrid UV-DIW printing process, with the UV lamp being switched on for 1 s and set at three different light intensities, 70 mW cm^{-2}, 150 mW cm^{-2} and 270 mW cm^{-2} (red, blue and green dots, respectively). As shown in Fig. 3, if the UV light is not switched on during the third interval, the ink shows a strong thixotropic tendency by slowly recovering its initial viscosity value (~10^3 Pa s) only after 40 s. This behavior is consistent with the one conventionally reported for DIW inks [55] and it is probably linked to the high solid fraction (i.e., 50 vol%) and to the liquid-particle interactions. When the UV light is switched on, the viscosity profile gradually increases as the light intensity increases: since the exposure time was kept constant, the higher the UV intensity, the quicker the energy dose overcomes the critical energy required for the
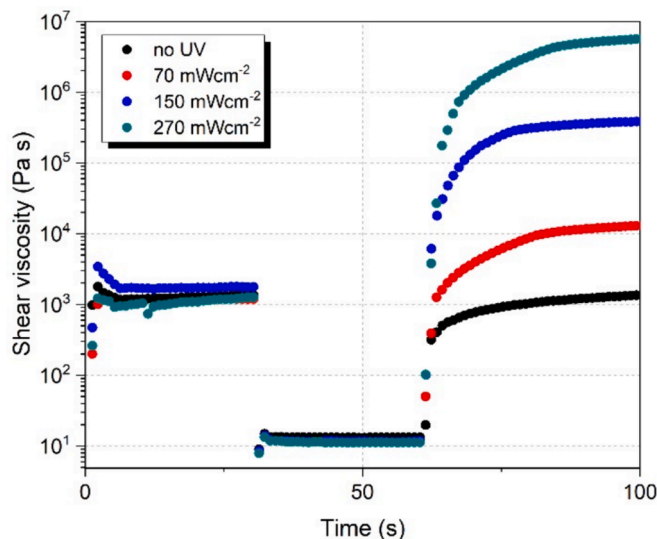

Fig. 3. Three intervals thixotropy test (3ITT) on the Si_3N_4-based ink with different UV exposure intensities.

polymerization [54]. Nonetheless, the initial viscosity of the ink is reached and exceeded almost instantly for all tested UV intensities, thus suggesting that a UV LEDs array with an intensity of 70 mW cm^{-2} is enough to ensure the freeform ability of the system.

The development of a silicon nitride ink suitable for the UV-DIW technology serves to further validate one of the main advantages of this hybrid process, i.e., a limited influence of the RI mismatch and of the curing depth on the freeform ability of the technology. In fact, as reported in our previous works, low transmittance and low curing depth of the ink do not significantly influence the free-standing ability of the process [10,35]. Indeed, the hybrid UV-DIW technique does not require a full cure of the extruded filament in order to guarantee its shape retention; the polymerization of the outer skin does suffice.

3.2. Lattices fabrication and characterization

With the aim to investigate the mechanical properties of the lattices through flexural testing, a beam structure was designed with dimensions (after sintering and consequent volumetric shrinkage measured from sintered samples from preliminary tests) according to the normative EN 843–1:2006 [56]. The structure was designed with a zig-zag pattern (Fig. 4 (a)) similar to what proposed by Warren et al. for the construction
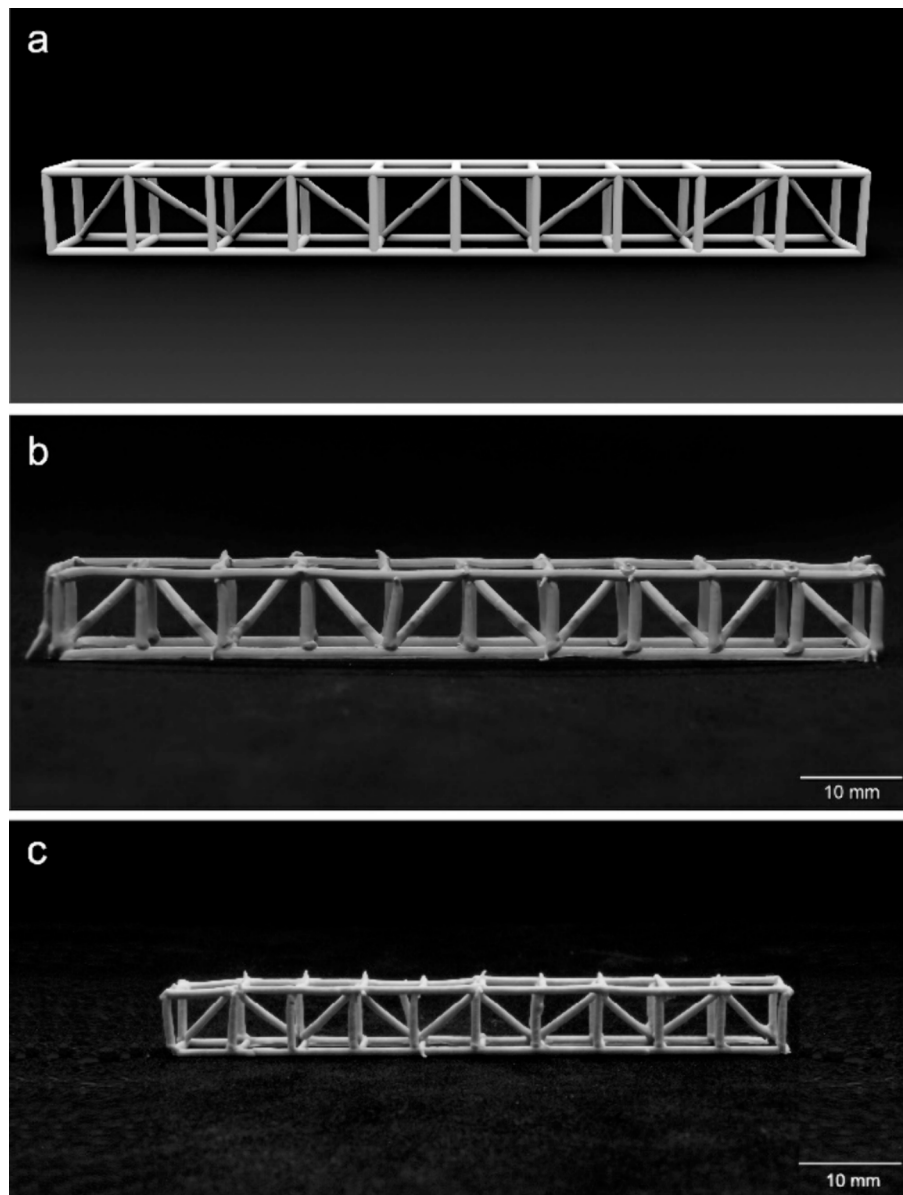
Fig. 4. Comparison between (a) CAD model, (b) as-printed and (c) sintered truss-made beam.

of suspended truss-made bridges [57]. Its nominal dimensions were 80 x 8 x 8 mm^3 (l x h x w) with an overall porosity of 91 % and resulted from the repetition of BCC unit cells (h x w) – alternatively mirrored along the beam length direction – with a strut thickness of 0.84 mm, corresponding to a theoretical aspect ratio ν of 0.105 ($\nu = \Phi/h$).

Fig. 4 (b) shows a lattice beam after printing and consisting of 58 different trusses, each of which was printed at 0.7 mm s^{-1} (v) and with an orientation of the printing head with respect to the vertical direction of 25° (α). The relatively low printing speed was selected in order to assure the fast increase of the ink rigidity through the printing process, thus allowing for the fabrication of all the different support-less features composing the beam structure (i.e., 90°, 0° and 45° inclined trusses with respect to the vertical direction) [58]. As per the head orientation, despite the high degree of freedom offered by the robot arm, it was not possible to perfectly match it with the truss axes, as it would have resulted in its collision with either the rest of the printed structure or the building plate [10].

Fig. 4 shows a good resemblance of the as-printed structure with the CAD model: the measured truss thickness is 0.87 ± 0.04 mm, while the angle formed by the inclined trusses is 45.4 ± 0.6°, thus confirming an

adequate matching between the printing speed, ink flow rate and curing rate.

Fig. 5 reports the cross-section of 3 trusses printed (extruded and cured) at different inclinations, i.e., 90°, 0° and 45° (Fig. 5 (a-c)). As expected, while freeform ability was demonstrated, all cross-sections reveal the presence of an outer skin with a thickness that corresponds to the measured curing depth. Moreover, differences in the cured thickness can be detected, suggesting a non-uniform irradiation of the filaments during printing; the phenomenon is particularly visible in the case of the horizontally inclined trusses (i.e., 90°, Fig. 5 (a)). Indeed, this is the result of the constant orientation of the printing head with respect to the vertical direction (i.e., $\alpha = 25°$) and, additionally, on the top-down projection of the UV light emitted by the diodes: since the printing head cannot rotate upside-down, the upper part of the filament (i.e., referred to the half of the cylindrical surface of the extruded filament closer to the UV diodes) will be constantly irradiated through the printing path, while the curing degree of the other half of the filament surface (hereafter referred to as bottom) will depend on the angular distance between the truss axis and the printing head. In particular, the higher the angle, the farther away will be the UV light with respect to the bottom surface of
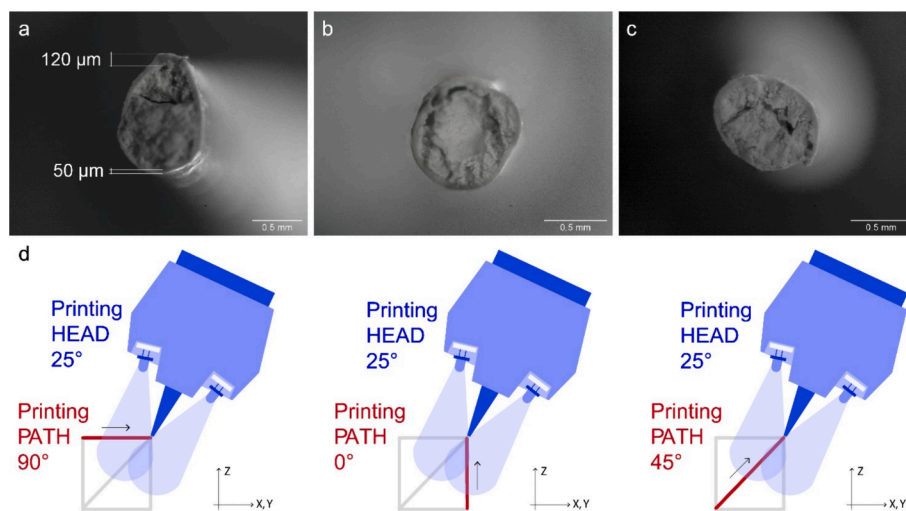
Fig. 5. Cross-section of different (extruded and cured) trusses of the beam structure: (a) horizontal, (b) vertical, (c) inclined (45°); for all reported pictures, the z axis is parallel to the cross-section and pointing upwards. Graphical representation of the differential curing during printing (d).

the filament and, consequently, the less homogeneously cured will be its cross-section.

Indeed, a similar result has been also recently discussed by Clarkson et al. [47]: by using a 3-axis UV-DIW printing setup and following a planar printing path, the curing depth on the bottom of the filament will be lower compared to the one on the top due to the high angular distance (i.e., 90°). Similarly to what described there, the horizontally inclined trusses reported in this work shows a differential curing between top and bottom of the filament cross-section (as highlighted in Fig. 5 (a)), while the vertical and 45° inclined trusses present an outer skin with a uniform thickness, as the angular distance is reduced (i.e., 65°, 25° and 20° for the horizontal, vertical and inclined trusses, respectively). Despite such non-uniform thickness, the successful fabrication of the truss-beam demonstrates that the curing depth is not a limiting factor for the UV-DIW technique, but it is rather the rapid reaction of the ink to UV light exposure that constitutes the critical parameter (Fig. 3).

3.3. Heating treatment and mechanical behavior

After printing, debinding and sintering treatments were performed to remove the organic phase (TMPTA, POE) and reach complete densification. As is well known, the post treatment of green samples is the most critical step in the fabrication of ceramic components starting from photocurable suspensions [59,60]. The TGA curve of the silicon nitride ink was taken as a reference to optimize the heating profile (Figure SI 7). As confirmed by the peaks in the derivative curve, the total weight loss (25.8 %) of the sample occurs in three steps: the first peak at 160 °C corresponds to the evaporation of POE, while the further loss in weight (~16 %) can be attributed to the condensation of the silanol groups of GLYMO (370 °C) and to the almost complete removal of TMPTA, which presents a 96 wt% loss at 450 °C [61,62]. The resulting ceramic yield (74.2 wt%) is close to the theoretical one (74.7 wt%) and corresponds to the initial amount of silicon nitride (73.9 wt%) plus the carbonaceous yield of TMPTA (0.8 wt%, i.e., 4 wt% of the initial amount of acrylate).

Fig. 4 (c) shows that the sample retained a good shape after the heat treatment, indicating that the removal of the organics and sintering did not lead to sagging or distortions of the beam structure.

Density and open porosity of the component were calculated according to the Archimedes principle; the values are reported in Table 2. The measured apparent density is of 3.05 ± 0.05 g cm^{-3}, which corresponds to a relative density of 95 % with respect to typical values for silicon nitride (i.e., 3.2 g cm^{-3}). This can be attributed to the limited curing depth of the silicon nitride ink highlighted in the previous section

Table 2

Density, porosity, mass loss, and shrinkage of sintered silicon nitride components.

Bulk density (g cm^{-3})	Apparent density (g cm^{-3})	Mass loss (%)	Volumetric shrinkage (%)
2.97 ± 0.08	3.05 ± 0.05	27.8 ± 2.4	49.1 ± 7.8

and showed in Fig. 5 (a-c): only a small fraction of filament cross-section actually cures during the printing process, thus leaving the core part of the truss still with un-reacted monomers. During the debinding step, the residual photoinitiator can act as a thermal initiator, thus leading to polymerization of the residual monomers in the core part of the truss [60]. In this way, additional heat is generated (the reaction is exothermic), causing a local increase in the temperature and the subsequent higher decomposition rate of the inner part with respect to the outer shell. As a result, the gases from the degradation of the monomers remain partially blocked inside the cured skin, leading to enclosed porosities which cannot later be completely eliminated during sintering. This was further confirmed by analyzing the cross-section of sintered filaments through SEM analysis: as reported in Fig. 6 (a), a discrete gradient of porosity is visible by moving from the (dense) skin of the filament to the (more porous) center, thus proving the inhibited gas release in the un-cured part.

Additionally, differences between the bulk and apparent density (Table 2) suggest the presence of open porosity. This was confirmed by analyzing the surface around the nodes of the structure. As shown in Fig. 6 (b), cracks formed in different parts of the structure, particularly in correspondence of the connection points between trusses. Indeed, this could be associated to the densification process during the sintering phase: since the geometry is constrained, the stresses generated during the sintering step and shrinkage of the sample will create a differential stress status between the nodes and the trusses, thus leading to the cracks. Moreover, it should be pointed out that Si_3N_4 particles and the glassy phase formed by the sintering aids (i.e., Al_2O_3 and Y_2O_3) represent the main contribution to the final ceramic yield; in this sense, no additional source is able to compensate for the high volumetric shrinkage (i.e., 49.1 ± 7.8 %), thus leading way to the formation of defects. A possible solution to this problem could be the one proposed by Clarkson et al. [47], which introduced a carbon-rich SiC forming preceramic polymer in a silicon nitride suspension: thanks to its excellent ceramic conversion, lower shrinkage (17.6 – 27.9 % assuming isotropic shrinkage [47]) and higher ceramic yield can be reached, ultimately
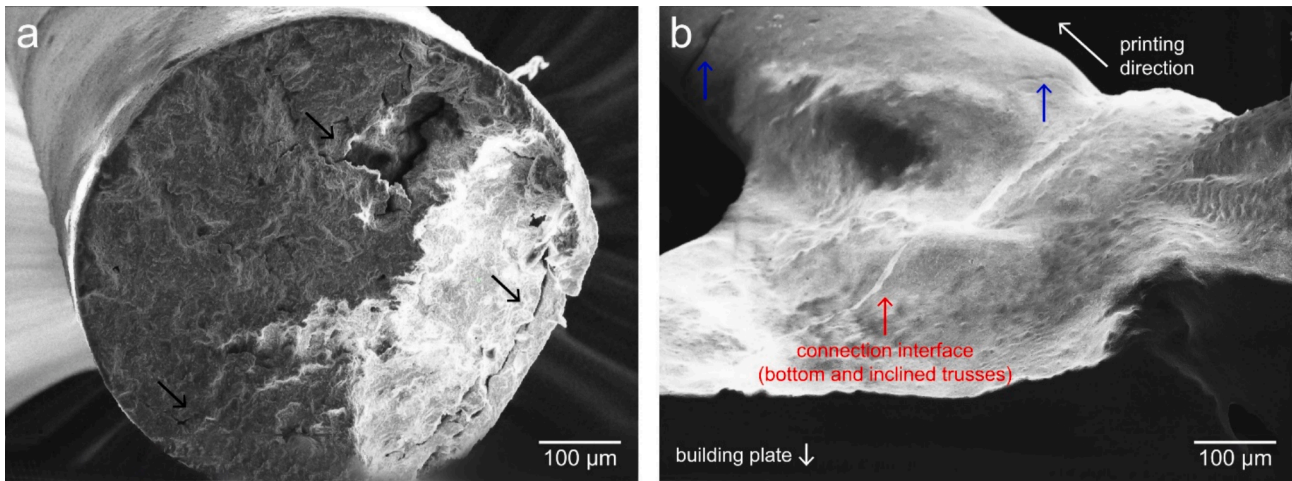
Fig. 6. SEM images of (a) the cross-section of a sintered filament (with black arrows pointing to pores between the skin and core of the filament) and, (b) the connection point between a horizontal and an inclined truss (with blue arrows pointing to cracks at the connection points between struts); the position of the building plate, the printing direction and the interface between the bottom and inclined trusses are highlighted.

resulting in a 99 % relative density after sintering.

The XRD profile of the sintered sample reported in Figure SI 1 (b) shows the presence of β-Si_3N_4, Y_2O_3 and Al_2O_3 phases, resulting from the precipitation and dissolution of the α-phase in a glassy matrix filled with acicular grains [63]. The sintering process of silicon nitride is a viscous-sintering process which is driven by the presence and reaction between the sintering aids (i.e., yttrium and alumina oxides) with the silicon oxide present on the surface of the silicon nitride particles [64]. Such interaction creates a liquid phase which coats the β-Si_3N_4 grains and remains as secondary phase after sintering, as confirmed by the SEM image shown in Fig. 7.

Once sintered (Fig. 4 (c)), lattice-beams were subjected to 4-point bending test. Samples having cross-section were placed on two supporting pins equally distanced (L/4, with L = 40 mm) from two loading pins which were moved down at a constant rate of 0.7 mm min^{-1} until failure of the sample.

The measured fracture load (F) can be described through the Weibull distribution (4), which represents the probability density function for strength variables:

$$f\left(\frac{F}{F_0}\right) = \frac{m}{F_0}\left(\frac{F}{F_0}\right)^{m-1} \exp\left[-\left(\frac{F}{F_0}\right)^m\right] \qquad (4)$$

Where m is the Weibull modulus and F_0 is a normalizing parameter. Through the linear-regression method [65] it is possible to plot the

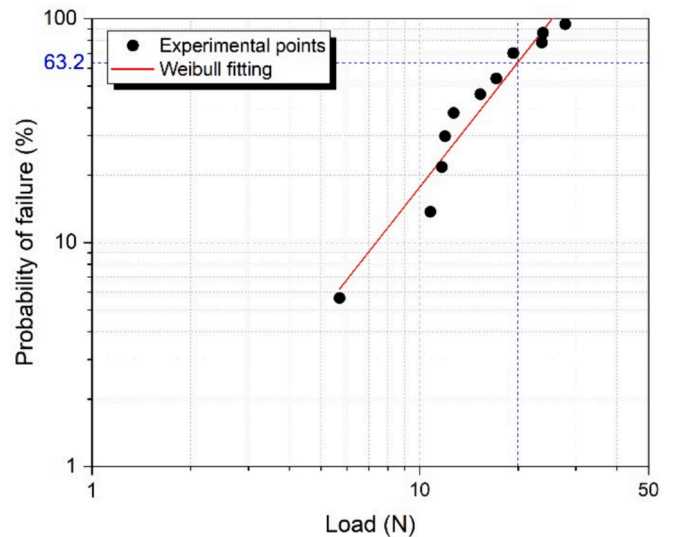fracture load values as a function of their probability of failure (P), thus

Fig. 8. Weibull graph from bending test performed on 11 lattice beams samples.
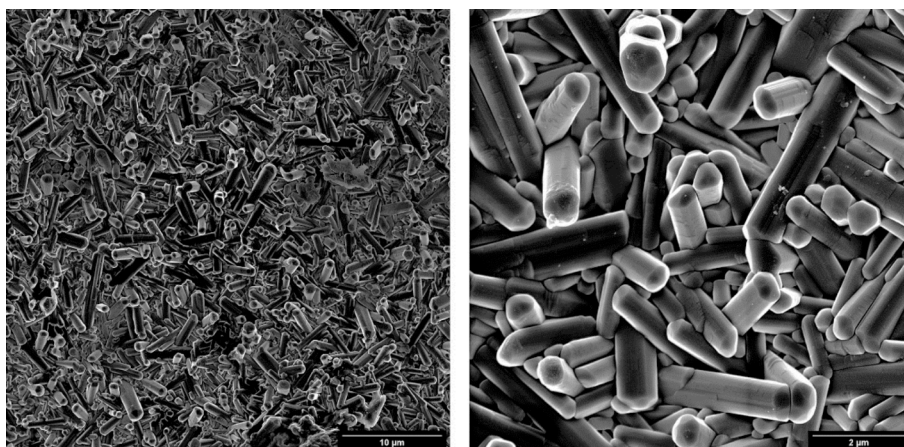

Fig. 7. SEM images of the surface of a sintered filament at 15000 X (left) and 72500 X (right).

obtaining the graph shown in Fig. 8, which reports the statistical distribution of the measured failure load of 11 different samples. By fitting of a linear curve, it is possible to estimate m (i.e., slope of the curve) and F_0 – instead, representing the characteristic failure load – which is the y-intercept at P = 63.2 %, thus obtaining characteristic values of m = 2.5 ± 0.2 and F = 18.4 ± 0.7 N (R^2 = 0.95). As the Weibull modulus is a measure of the mechanical reliability of the tested specimens, high values (i.e., m ~ 20) should be preferred, thus indicating a narrow defects size population [66]. Nonetheless, as previously reported, the differences associated with printing deviations from the CAD file, the presence of closed pores from air/gas pockets (Fig. 5) and/or cracks in correspondence of the connection points (Fig. 7) all make the distribution of defects quite wide and non-homogeneous, resulting in significant variance in the critical load and final deformation of the samples (see Figure SI 4). Moreover, as demonstrated by Keles et al. [67], low values of m (i.e., m < 10) are generally expected for highly porous (i.e., > 50 %) ceramics – as the lattice beams here investigated.

3.4. Results of the FE simulations and the application of a LEFM-based approach

Fig. 9 shows the total deformation of the lattice structure subjected to 4-point bending loading, as calculated by solving the FE model defined in Figure SI 6. As expected, the lattice structure mainly deforms due to bending loading in the XY plane; moreover, Fig. 9 highlights that the bending deformation on the XY plane provokes a bending deformation also on XZ plane due to the anisotropy of the unit cell of the lattice structure.

Fig. 10 (a, b) shows the plot of the maximum principal stress derived by solving the FE model having element size d = 0.2 mm. The zoom highlights the critical location at one node of the structure, where the singular maximum principal stress is $\sigma_{11,max} = \sigma_{peak} = 458$ MPa, which is approximately equal to 454 MPa derived from equation (SI 6). The corresponding reaction force R_y is equal to 42.57 N, which has been defined as the numerically estimated failure load. It is worth highlighting that such critical location of the peak stress is consistent with the experimental result, as reported in Fig. 10 (c).

The same procedure has been repeated also for the FE model having element size d = 0.1 mm: a singular maximum principal stress $\sigma_{11,max} = \sigma_{peak} = 619$ MPa, which is approximately equal to 622 MPa derived from equation (SI 6), has been calculated at one node of the structure when the corresponding reaction force R_y resulted equal to 36.33 N. By considering that the parameter K^*_{FE} in equation (SI 6) assumes a constant value but with a deviation of ± 15 %, it can be concluded that the numerically estimated failure loads are:

- 42.57 N ± 15 %, which means between 36.18 N and 48.96 N, for the case d = 0.2 mm;
- 36.33 N ± 15 %, which means between 30.88 N and 41.78 N, for the case d = 0.1 mm.

The ranges of failure loads have an overlapping region; therefore the convergence of the results is confirmed and the average failure load can be estimated in (36.18 + 41.78)/2 = 39 N. Such result is higher than the average failure load derived from the experimental tests, being equal to F = 18.4 N according to Weibull's analysis. However, this can be justified by the fact that the FE model represents the ideal geometry of the lattice beam structure, in terms of shape and local dimensions, thus not accounting for (i) the limited curing depth (see Fig. 5), (ii) the defects introduced by the printing method, such as discontinuities in the truss shape (i.e., enlarged extremities), interfaces and air gaps on nodes, as observed in Fig. 6, and, (iii) distortions of the beam structures due to thermal induced stresses; all of them being detrimental for the strength of the lattice structure.

4. Conclusions

The research presented in this paper demonstrates the successful formulation of a silicon nitride-based ink suitable for the UV-DIW technique, possessing a shear-thinning behavior and rapid consolidation upon UV irradiation. Increased dispersion of the particles was reached thanks to the optimization of particles size distribution and the introduction of a silane compound to act as steric agent, thus maximizing the packing density of the system. Albeit the high refractive index of silicon nitride makes it hardly printable via vat-photopolymerization techniques, the poor curing depth did not compromise the fabrication of freeform geometries; this further demonstrated that the UV-DIW technology is able to effectively overcome the light-particle interaction issue, thus enabling the fabrication of complex and ultra-lightweight truss-based structures with high fidelity. Nevertheless, the limited curing depth could not be fully overcome, thus resulting in the presence of some closed pores and cracks upon thermal treatment, negatively affecting the final mechanical properties of the sintered structures. From such perspectives, different approaches could be considered to overcome these issues. The first would require the additional optimization of the ink design: the introduction of preceramic precursors or the further modification of the silicon nitride particle surface (i.e., by oxidation) could allow the reduction of the refractive index mismatch and achieve a higher density of the sintered structures [47]. Contextually, employing a different curing mechanism could be beneficial to prevent the generation of cracks. Dual-curing, for example, combines two polymerization processes in one formulation, activated either simultaneously or sequentially using UV light and temperature,
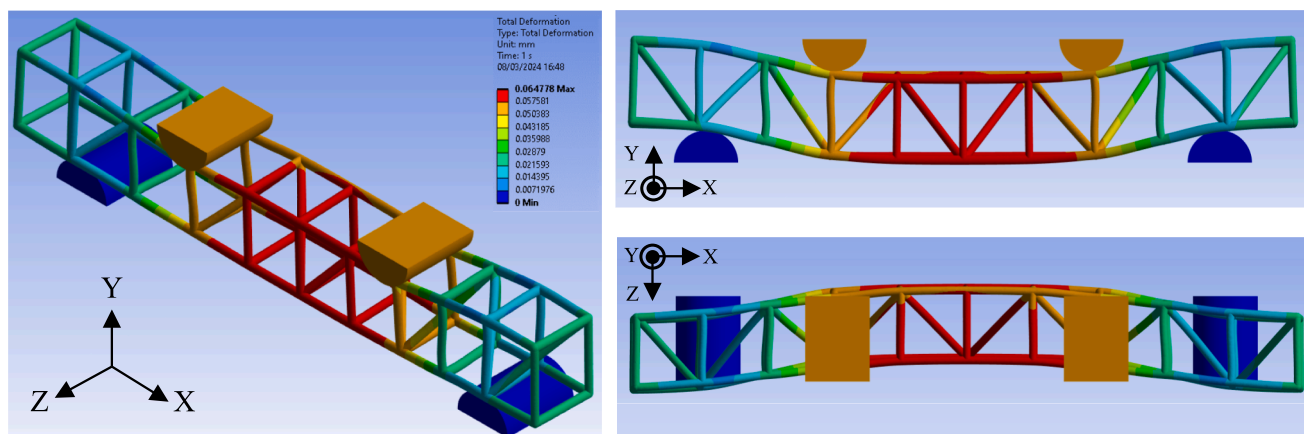

Fig. 9. Total deformation of the lattice structure calculated by solving the FE model of Figure SI 5.
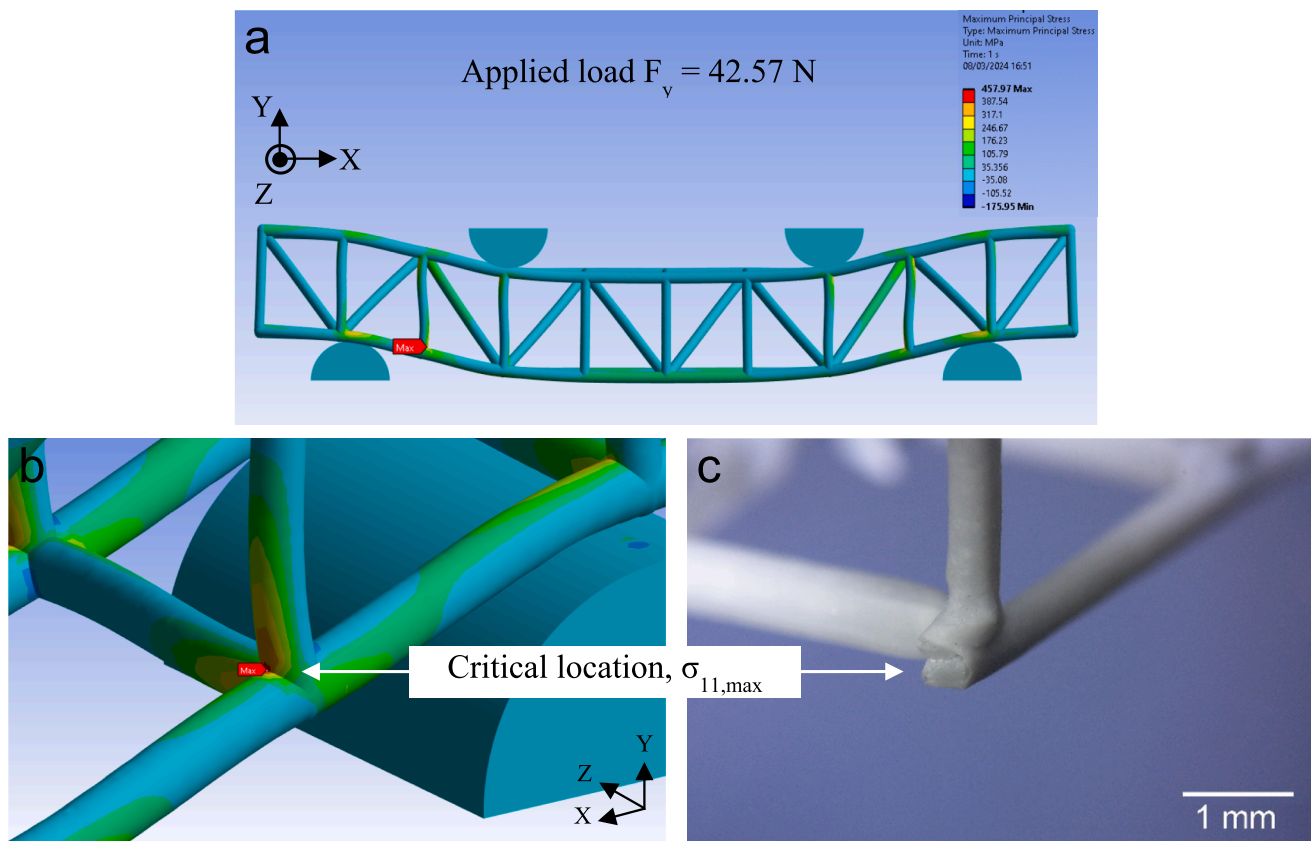
Fig. 10. Plot of the maximum principal stress (a); zoom of the critical location of the lattice structure resulting by solving the FE model of Figure SI 5 with $d = 0.2$ mm (b) and its correspondence in a sintered truss-based beam after the experimental 4-point bending test (c).

thus allowing for the homogeneous curing of the whole truss section and avoiding the generation of differential decomposition rates [68]. Another way to overcome the high absorption of UV light of ceramics is the use of a near-infrared (NIR) irradiation system coupled with up-conversion particles (UCPs): upon irradiation at NIR wavelengths, excited UCPs emit UV–visible fluorescence, thus acting as internal light sources inside of the ink and allowing its rapid curing [69]. It should be noted, though, that UCPs require a high energy dose to be activated, i.e., high power lasers far more expensive and less compact than the UV-LED diodes employed in this work should be used.

Mechanical testing and finite element simulations provided insights into the structural integrity and load-bearing capacity of the printed structures. Another reason for the low failure load obtained from the experimental tests, which is taken into account by the FE simulations, is due to the combination of the external load with a non-symmetric structure with respect to XY plane (see Fig. 9). In fact, bending deformation on XY plane provokes bending deformation also on XZ plane due to the anisotropy of the unit cell of the truss-based structure. From this perspective, the design of a symmetric lattice is expected to increase the experimental as well as the numerical failure load, since it will remove the coupled bending deformation on the XZ plane. For this aim, the FE simulations coupled with the LEFM-based approach will be helpful in the optimization of the lattice structure design.

Moving forward, addressing challenges related to ink composition, curing depth uniformity, and post-processing-induced defects will be crucial for enhancing the mechanical performance of printed structures and unlocking the full potential of this AM approach in fabricating complex and high-performance ceramic components for diverse engineering applications especially as lightweight structures for harsh environments (i.e., supports for MEMS mirrors or other aerospace equipment).

CRediT authorship contribution statement

Anna De Marzi: Writing – original draft, Visualization, Validation, Software, Methodology, Investigation, Data curation. **Sarah Diener:** Writing – review & editing, Investigation. **Alberto Campagnolo:** Writing – original draft, Validation, Software, Formal analysis. **Giovanni Meneghetti:** Writing – review & editing, Validation. **Nikolaos Katsikis:** Funding acquisition. **Paolo Colombo:** Writing – review & editing, Supervision, Resources, Funding acquisition. **Giorgia Franchin:** Writing – review & editing, Supervision, Conceptualization.

Declaration of competing interest

The authors declare the following financial interests/personal relationships which may be considered as potential competing interests: Paolo Colombo, Nikolaos Katsikis reports financial support was provided by European Commission. Anna De Marzi reports financial support was provided by European Commission. If there are other authors, they declare that they have no known competing financial interests or personal relationships that could have appeared to influence the work reported in this paper.

Data availability

Data will be made available on request.

Appendix A. Supplementary data

Supplementary data to this article can be found online at https://doi.org/10.1016/j.matdes.2024.113092.

References

[1] F.W. Zok, R.M. Latture, M.R. Begley, Periodic truss structures, J. Mech. Phys. Solids 96 (Nov. 2016) 184–203, https://doi.org/10.1016/J.JMPS.2016.07.007.

[2] J. Bauer, S. Hengsbach, I. Tesari, R. Schwaiger, O. Kraft, High-strength cellular ceramic composites with 3D microarchitecture, Proc. Natl. Acad. Sci. U. S. A. 111 (7) (Feb. 2014) 2453–2458, https://doi.org/10.1073/PNAS.1315147111/SUPPL_FILE/SM04.MP4.

[3] X. Zheng, et al., Ultralight, ultrastiff mechanical metamaterials, Science 80-.), 344 (6190 (Jun. 2014) 1373–1377, https://doi.org/10.1126/SCIENCE.1252291/SUPPL_FILE/ZHENG.SM.PDF.

[4] V.B. John, The Shaping of Materials, in: Introduction to Engineering Materials, Palgrave Macmillan, London, 1983, pp. 137–177, https://doi.org/10.1007/978-1-349-17190-3_8.

[5] B. DeBoer, N. Nguyen, F. Diba, A. Hosseini, Additive, subtractive, and formative manufacturing of metal components: a life cycle assessment comparison, Int. J. Adv. Manuf. Technol. 115 (1–2) (Jul. 2021) 413–432, https://doi.org/10.1007/S00170-021-07173-5.

[6] D. D. Camacho *et al.*, "Applications of Additive Manufacturing in the Construction Industry - A Prospective Review," in *34th International Symposium on Automation and Robotics in Construction*, 2017. doi: 10.22260/ISARC2017/0033.

[7] K.C. Cheung, N. Gershenfeld, Reversibly Assembled Cellular Composite Materials, Science 80-.), 341(6151 (Sep. 2013) 1219–1221, https://doi.org/10.1126/science.1240889.

[8] L. Dong, V. Deshpande, H. Wadley, Mechanical response of Ti–6Al–4V octet-truss lattice structures, Int. J. Solids Struct. 60–61 (May 2015) 107–124, https://doi.org/10.1016/j.ijsolstr.2015.02.020.

[9] I. Gibson, D. Rosen, B. Stucker, and M. Khorasani, *Additive Manufacturing Technologies*. 2021.

[10] A. De Marzi, M. Vibrante, M. Bottin, G. Franchin, Development of robot assisted hybrid additive manufacturing technology for the freeform fabrication of lattice structures, Addit. Manuf. 66 (Mar. 2023) 103456, https://doi.org/10.1016/j.addma.2023.103456.

[11] G. Schuh, J. Kreysa, S. Orilski, 'hybrid production' road map, Zeitschrift Fuer Wirtschaftlichen Fabrikbetr. 104 (5) (May 2009) 385–391, https://doi.org/10.3139/104.110072.

[12] K. Huang, A. De Marzi, G. Franchin, P. Colombo, UV-assisted Robotic Arm Freeforming of SiOC Ceramics from a Preceramic Polymer, Addit. Manuf. (Feb. 2024) 104051, https://doi.org/10.1016/j.addma.2024.104051.

[13] Z. Krstic, V.D. Krstic, "silicon Nitride: the Engineering Material of the Future" 47 (2) (Jan. 2012), https://doi.org/10.1007/s10853-011-5942-5.

[14] S. Hampshire, Silicon nitride ceramics-review of structure, processing and properties, J. Achiev. Mater. Manuf. Eng. 24 (1) (2007) 43–50.

[15] H. Klemm, Silicon Nitride for High-Temperature Applications, J. Am. Ceram. Soc. 93 (6) (Jun. 2010) 1501–1522, https://doi.org/10.1111/J.1551-2916.2010.03839.X.

[16] X. Du, S.S. Lee, G. Blugan, S.J. Ferguson, Silicon Nitride as a Biomedical Material: An Overview, Int. J. Mol. Sci. 23 (12) (Jun. 2022), https://doi.org/10.3390/IJMS23126551.

[17] W. Wijianto, Application of Silicon Nitride (Si3N4) Ceramics in Ball Bearing, Media Mesin Maj. Tek. Mesin 15 (1) (Aug. 2016), https://doi.org/10.23917/MESIN.V15I1.2296.

[18] X. Dong, et al., Additive manufacturing of silicon nitride ceramics: A review of advances and perspectives, Int. J. Appl. Ceram. Technol. no. July (2022) 2929–2949, https://doi.org/10.1111/ijac.14162.

[19] S. Yu, et al., Fabrication of Si3N4–SiC/SiO2 composites using 3D printing and infiltration processing, Ceram. Int. 47 (20) (Oct. 2021) 28218–28225, https://doi.org/10.1016/J.CERAMINT.2021.06.235.

[20] S. Rangarajan, G. Qi, N. Venkataraman, A. Safari, S.C. Danforth, Powder Processing, Rheology, and Mechanical Properties of Feedstock for Fused Deposition of Si3N4 Ceramics, J. Am. Ceram. Soc. 83 (7) (Jul. 2000) 1663–1669, https://doi.org/10.1111/J.1151-2916.2000.TB01446.X.

[21] H. Jin, D. Jia, Z. Yang, Y. Zhou, Direct ink writing of Si2N2O porous ceramic strengthened by directional β-Si3N4 grains, Ceram. Int. 46 (10) (Jul. 2020) 15709–15713, https://doi.org/10.1016/J.CERAMINT.2020.03.077.

[22] Y. Liu, et al., Formation mechanism of stereolithography of Si3N4 slurry using silane coupling agent as modifier and dispersant, Ceram. Int. 46 (10) (Jul. 2020) 14583–14590, https://doi.org/10.1016/j.ceramint.2020.02.258.

[23] X.X. Li, et al., Rheology and Curability Characterization of Photosensitive Slurries for 3D Printing of Si3N4 Ceramics, Appl. Sci. 10 (18) (Sep. 2020) 6438, https://doi.org/10.3390/app10186438.

[24] M. S. Faria, F. J. Oliveira, C. M. Fernandes, D. Figueiredo, and S. Olhero, "Si3N4 Parts Fabricated by Robocasting: Proof of Concept," in *MATERIAIS 2022*, Jun. 2022, vol. 8, no. 1, p. 67. doi: 10.3390/materproc2022008067.

[25] S. Iyer, et al., Microstructural Characterization and Mechanical Properties of Si 3 N 4 Formed by Fused Deposition of Ceramics, Int. J. Appl. Ceram. Technol. 5 (2) (Mar. 2008) 127–137, https://doi.org/10.1111/j.1744-7402.2008.02193.x.

[26] S. Diener, et al., X-ray microtomography investigations on the residual pore structure in silicon nitride bars manufactured by direct ink writing using different printing patterns, Open Ceram. 5 (Mar. 2021) 100042, https://doi.org/10.1016/J.OCERAM.2020.100042.

[27] W.J. Costakis, et al., Material extrusion of highly-loaded silicon nitride aqueous inks for solid infilled structures, Addit. Manuf. 64 (Feb. 2023) 103425, https://doi.org/10.1016/j.addma.2023.103425.

[28] Z. Huang, et al., Stereolithography 3D printing of Si3N4 cellular ceramics with ultrahigh strength by using highly viscous paste, Ceram. Int. 49 (4) (Feb. 2023) 6984–6995, https://doi.org/10.1016/j.ceramint.2022.10.137.

[29] F. Berto, P. Lazzarin, Recent developments in brittle and quasi-brittle failure assessment of engineering materials by means of local approaches, Mater. Sci. Eng. R Reports 75 (Jan. 2014) 1–48, https://doi.org/10.1016/j.mser.2013.11.001.

[30] G. Meneghetti, P. Lazzarin, Significance of the elastic peak stress evaluated by FE analyses at the point of singularity of sharp V-notched components, Fatigue Fract. Eng. Mater. Struct. 30 (2) (Feb. 2007) 95–106, https://doi.org/10.1111/j.1460-2695.2006.01084.x.

[31] G. Meneghetti, A. Campagnolo, State-of-the-art review of peak stress method for fatigue strength assessment of welded joints, Int. J. Fatigue 139 (Oct. 2020) 105705, https://doi.org/10.1016/j.ijfatigue.2020.105705.

[32] M.D. Abramoff, P.J. Magalhaes, S.J. Ram, Image processing with ImageJ, Biophotonics Int. 11 (7) (2004) 36–42.

[33] M.B. Berger, "The importance and testing of density/porosity/permeability/pore size for refractories", in, Conference of the Southern African Institute of Mining and Metallurgy Refractories 2010 (2010) 101–116.

[34] D.N. Prabhakar Murthy, M. Xie, R. Jiang, Weibull Models, July. Wiley 2 (2003) no, https://doi.org/10.1002/047147326X.

[35] A. De Marzi, G. Giometti, J. Erler, P. Colombo, and G. Franchin, "Hybrid additive manufacturing for the fabrication of freeform transparent silica glass components," *Addit. Manuf.*, vol. 54, no. March, p. 102727, 2022, doi: 10.1016/j.addma.2022.102727.

[36] L.L. Lebel, B. Aissa, M.A. El Khakani, D. Therriault, Ultraviolet-Assisted Direct-Write Fabrication of Carbon Nanotube/Polymer Nanocomposite Microcoils, Adv. Mater. 22 (5) (Feb. 2010) 592–596, https://doi.org/10.1002/ADMA.200902192.

[37] R.P. Chhabra, J.F. Richardson, Non-Newtonian flow in the process industries : fundamentals and engineering applications, Butterworth-Heinemann (1999), https://doi.org/10.1016/B978-0-7506-3770-1.X5000-3.

[38] J.W. Halloran, M.L. Griffith, Ultraviolet Curing of Highly Loaded Ceramic Suspensions for Stereolithography of Ceramics, Am. Soc. Mech. Eng. Prod. Eng. Div. 68 (2) (1994) 529–534, https://doi.org/10.15781/T2599ZM4Q.

[39] J.N. Israelachvili, *Intermolecular and Surface Forces*. Academic Press (2011), https://doi.org/10.1016/C2009-0-21560-1.

[40] M. Wozniak, T. Graule, Y. de Hazan, D. Kata, J. Lis, Highly loaded UV curable nanosilica dispersions for rapid prototyping applications, J. Eur. Ceram. Soc. 29 (11) (Aug. 2009) 2259–2265, https://doi.org/10.1016/j.jeurceramsoc.2009.01.030.

[41] J. Kizling, B. Kronberg, and J. C. Eriksson, "On the formation and stability of high internal phase O/W emulsions," *Adv. Colloid Interface Sci.*, vol. 123–126, no. SPEC. ISS., pp. 295–302, Nov. 2006, doi: 10.1016/J.CIS.2006.05.006.

[42] M. Börjesson, G. Richardson, G. Westman, UV radiation of cellulose fibers and acrylic acid modified cellulose fibers for improved stiffness in paper, Bio Resources 10 (2) (2015) 3056–3069, https://doi.org/10.15376/BIORES.10.2.3056-3069.

[43] Y. Liu, et al., Effects of particle size and color on photocuring performance of Si3N4 ceramic slurry by stereolithography, J. Eur. Ceram. Soc. 41 (4) (Apr. 2021) 2386–2394, https://doi.org/10.1016/J.JEURCERAMSOC.2020.11.032.

[44] M. DeLombard-Watts, P.T. Weissman, Comparison of performance of acrylate and methacrylate aliphatic urethanes, RadTech Proc. (2004).

[45] R.-J. Huang, et al., Fabrication of complex shaped ceramic parts with surface-oxidized Si3N4 powder via digital light processing based stereolithography method, Ceram. Int. 45 (4) (Mar. 2019) 5158–5162, https://doi.org/10.1016/j.ceramint.2018.11.116.

[46] E. Schwarzer-Fischer, et al., CerAMfacturing of silicon nitride by using lithography-based ceramic vat photopolymerization (CerAM VPP), J. Eur. Ceram. Soc. 43 (2023) 321–331, https://doi.org/10.1016/j.jeurceramsoc.2022.10.011.

[47] C.M. Clarkson, C. Wyckoff, M.J.S. Parvulescu, L.M. Rueschhold, M.B. Dickerson, UV-assisted direct ink writing of Si3N4/SiC preceramic polymer suspensions, J. Eur. Ceram. Soc. 42 (8) (Jul. 2022) 3374–3382, https://doi.org/10.1016/J.JEURCERAMSOC.2022.03.001.

[48] M. Wang, et al., Polymer-derived silicon nitride ceramics by digital light processing based additive manufacturing, J. Am. Ceram. Soc. 102 (9) (Sep. 2019) 5117–5126, https://doi.org/10.1111/JACE.16389.

[49] W. Zou, P. Yang, L. Lin, Y. Li, S. Wu, Improving cure performance of Si3N4 suspension with a high refractive index resin for stereolithography-based additive

manufacturing, Ceram. Int. 48 (9) (May 2022) 12569–12577, https://doi.org/10.1016/J.CERAMINT.2022.01.124.

[50] P.F. Jacobs, Rapid prototyping & manufacturing : fundamentals of stereolithography, Soc. Manuf. Eng. Comput. Autom. Syst. Assoc. SME (1993) 434.

[51] M. Shen, et al., Effects of exposure time and printing angle on the curing characteristics and flexural strength of ceramic samples fabricated via digital light processing, Ceram. Int. 46 (15) (Oct. 2020) 24379–24384, https://doi.org/10.1016/J.CERAMINT.2020.06.220.

[52] X. Li, K. Hu, Z. Lu, Effect of light attenuation on polymerization of ceramic suspensions for stereolithography, J. Eur. Ceram. Soc. 39 (7) (Jul. 2019) 2503–2509, https://doi.org/10.1016/J.JEURCERAMSOC.2019.01.002.

[53] T. Chartier, et al., Influence of irradiation parameters on the polymerization of ceramic reactive suspensions for stereolithography, J. Eur. Ceram. Soc. 37 (15) (Dec. 2017) 4431–4436, https://doi.org/10.1016/J.JEURCERAMSOC.2017.05.050.

[54] F. Jiang, D. Drummer, "curing Kinetic Analysis of Acrylate Photopolymer for Additive Manufacturing by Photo-DSC", *Polymers (basel)* vol. 12 (2020) 1080, https://doi.org/10.3390/polym12051080.

[55] L. del-Mazo-Barbara and M.-P. Ginebra, "Rheological characterisation of ceramic inks for 3D direct ink writing: A review," *J. Eur. Ceram. Soc.*, vol. 41, no. 16, pp. 18–33, Dec. 2021, doi: 10.1016/j.jeurceramsoc.2021.08.031.

[56] British Standards, *Advanced technical ceramics : mechanical properties of monolithic ceramics at room temperature. Part 1, Determination of flexural strength*. 2006, p. 24.

[57] F. J. Griggs, "The Warren Truss," Structure, pp. 44–48, 2015.

[58] R.D. Farahani, L.L. Lebel, D. Therriault, Processing parameters investigation for the fabrication of self-supported and freeform polymeric microstructures using ultraviolet-assisted three-dimensional printing, J. Micromechanics Microengineering 24 (5) (Apr. 2014) 055020, https://doi.org/10.1088/0960-1317/24/5/055020.

[59] E. Johansson, O. Lidström, J. Johansson, O. Lyckfeldt, E. Adolfsson, J. Stampfl, Influence of Resin Composition on the Defect Formation in Alumina Manufactured by Stereolithography, Materials (basel) 10 (2017) 138, https://doi.org/10.3390/ma10020138.

[60] C.J. Bae, J.W. Halloran, Influence of Residual Monomer on Cracking in Ceramics Fabricated by Stereolithography, Int. J. Appl. Ceram. Technol. 8 (6) (Nov. 2011) 1289–1295, https://doi.org/10.1111/J.1744-7402.2010.02578.X.

[61] S. Ek, Determination of the hydroxyl group content in silica by thermogravimetry and a comparison with 1H MAS NMR results, Thermochim. Acta 379 (1–2) (Nov. 2001) 201–212, https://doi.org/10.1016/S0040-6031(01)00618-9.

[62] J. Kim, C.W. Gal, Y.-J. Choi, H. Park, S.-Y. Yoon, H. Yun, Effect of non-reactive diluent on defect-free debinding process of 3D printed ceramics, Addit. Manuf. 67 (Apr. 2023) 103475, https://doi.org/10.1016/j.addma.2023.103475.

[63] H. Suematsu, M. Mitomo, T.E. Mitchell, J.J. Petrovic, O. Fukunaga, N. Ohashi, The α–β Transformation in Silicon Nitride Single Crystals, J. Am. Ceram. Soc. 80 (3) (Mar. 1997) 615–620, https://doi.org/10.1111/J.1151-2916.1997.TB02876.X.

[64] Y.I. Belyi, V.V. Koleda, V.M. Svistun, O.G. Kochetkova, L.V. Doroshenko, Liquid-phase sintering of a silicon nitride-based ceramic, Glas. Ceram. 48 (1) (1991) 24–26, https://doi.org/10.1007/bf00677727.

[65] J. C. Zhou and D. F. Wu, "Materials Science and Technology Estimation of Weibull parameters with linear regression method Estimation of Weibull parameters with linear regression method," 2013, doi: 10.1179/026708309X12459430509175.

[66] M.A. Meyers, K.K. Chawla, Mechanical Behavior of Materials, Cambridge University Press, 2008.

[67] Ö. Keleş, N.P. Barcenas, D.H. Sprys, K.J. Bowman, Effect of Porosity on Strength Distribution of Microcrystalline Cellulose, AAPS PharmSciTech 16 (6) (Dec. 2015) 1455–1464, https://doi.org/10.1208/S12249-015-0325-X.

[68] X. Fernández-Francos, O. Konuray, X. Ramis, À. Serra, S. De la Flor, Enhancement of 3D-Printable Materials by Dual-Curing Procedures, Materials (basel) 14 (1) (Dec. 2020) 107, https://doi.org/10.3390/ma14010107.

[69] Y. Zhao, J. Zhu, W. He, Y. Liu, X. Sang, R. Liu, 3D printing of unsupported multi-scale and large-span ceramic via near-infrared assisted direct ink writing, Nat. Commun. 14 (1) (Apr. 2023) 2381, https://doi.org/10.1038/s41467-023-38082-8.